Available online at www.sciencedirect.com
SCIENCE DIRECT®
Journal of Magnetic Resonance 176 (2005) 187–198
JMR Journal of Magnetic Resonance
www.elsevier.com/locate/jmr

Phase-constrained parallel MR image reconstruction

Jacob D. Willig-Onwuachi [a,*], Ernest N. Yeh [b,d], Aaron K. Grant [b], Michael A. Ohliger [b,d], Charles A. McKenzie [b], Daniel K. Sodickson [b,c,d]

[a] Departments of Radiology and Biomedical Engineering, University of California Davis, Davis, CA, USA
[b] Department of Radiology, Beth Israel Deaconess Medical Center and Harvard Medical School, Boston, MA, USA
[c] Department of Medicine, Cardiovascular Division, Beth Israel Deaconess Medical Center and Harvard Medical School, Boston, MA, USA
[d] Harvard-MIT Division of Health Sciences and Technology, Boston, MA, USA

Received 6 November 2004; revised 3 June 2005
Available online 18 July 2005

Abstract

A generalized method for phase-constrained parallel MR image reconstruction is presented that combines and extends the concepts of partial-Fourier reconstruction and parallel imaging. It provides a framework for reconstructing images employing either or both techniques and for comparing image quality achieved by varying *k*-space sampling schemes. The method can be used as a parallel image reconstruction with a partial-Fourier reconstruction built in. It can also be used with trajectories not readily handled by straightforward combinations of partial-Fourier and SENSE-like parallel reconstructions, including variable-density, and non-Cartesian trajectories. The phase constraint specifies a better-conditioned inverse problem compared to unconstrained parallel MR reconstruction alone. This phase-constrained parallel MRI reconstruction offers a one-step alternative to the standard combination of homodyne and SENSE reconstructions with the added benefit of flexibility of sampling trajectory. The theory of the phase-constrained approach is outlined, and its calibration requirements and limitations are discussed. Simulations, phantom experiments, and in vivo experiments are presented.

Keywords: Parallel imaging; Partial-Fourier; Constrained reconstruction; Coil arrays

1. Introduction

Parallel acquisition techniques [1–9] in magnetic resonance imaging (MRI) enable reductions in imaging time through the use of multiple receiver coils. Spatial information from the coils is used to replace a portion of the spatial encoding traditionally accomplished using magnetic field gradients. A reduced data set is collected and the data points that were omitted from the acquisition are effectively recovered by exploiting the separate coil "views."

Other techniques have also created images from reduced data sets. Constrained reconstructions [10], for example, effectively fill in *k*-space lines not acquired during the scan using a priori knowledge about the data or the object being imaged. Phase-constrained (commonly referred to in the literature and in this paper as "partial-Fourier") techniques, in particular, like the technique of Margosian et al. [11], homodyne detection [12], or Projection Onto Convex Sets (POCS) [13–16], exploit a known Hermitian data symmetry. These techniques use only half of *k*-space and a low-resolution phase map to reconstruct a full image.

There are many reasons to consider combining partial-Fourier and parallel MR. For example, by reducing imaging time, various combinations of these methods

* Corresponding Author. Fax: +1 916 734 0316.
E-mail address: jwillig@ucdavis.edu (J.D. Willig-Onwuachi).

1090-7807/$ - see front matter © 2005 Elsevier Inc. All rights reserved.
doi:10.1016/j.jmr.2005.06.004

have been demonstrated to improve the performance of real-time imaging [17], improve the spatial resolution of single-shot imaging [18,19], enable whole-heart coverage in a single breath-hold for calculation of the ejection fraction [20], and acquire whole brain three-dimensional susceptibility-weighted data in 0.5 s with a PRESTO sequence [21]. Despite these reasons, there are also potential pitfalls. Although combining partial-Fourier and parallel MR can be straightforward under certain prescribed circumstances, it is in general an interesting and non-trivial problem deserving closer examination.

Typically, the parallel MR and partial-Fourier reconstructions are performed in two (or more) separate steps. The type of parallel reconstruction being used, however, determines the order in which these steps must be performed. The most natural order, when using a "*k*-space" reconstruction like GRAPPA or SMASH, is to perform the parallel reconstruction first, followed by the partial-Fourier reconstruction. On the other hand, when using an "image-space" reconstruction like Cartesian SENSE, a partial-Fourier reconstruction or a zero-filling operation must be performed first to generate a regularly aliased image to unfold. One of the more robust algorithms uses homodyne detection and SENSE [22]. The homodyne partial-Fourier reconstruction [12] uses a 'conjugate doubling' and a phase correction, where the high frequency data on the acquired side of *k*-space is doubled to compensate for the missing signal power in the high frequency region on the skipped side of *k*-space. Alternative techniques for combining SENSE and partial-Fourier have only recently been discussed [23–26]. Also, the particular reconstruction scheme will determine the allowable *k*-space sampling patterns and the feasible methods for implementation, including measuring the phase map and coil sensitivities. The algorithm should be carefully planned for each new implementation because of the many variables involved.

In this paper, we describe a novel method of combining parallel MRI and phase-constrained concepts into a single reconstruction. This method can be used as an alternative to the homodyne SENSE technique or as a method of constraining the inversion for standard SENSE techniques. Additionally, the general formalism we present enables the reconstruction of a wide variety of undersampled datasets. We refer to this as a 'phase-constrained' parallel MRI reconstruction as opposed to a 'partial-Fourier' parallel MRI reconstruction, because it can be applied to data that is symmetric (as opposed to asymmetric or one-sided) in nature. It can be used more generally to *constrain* or improve the matrix inversion for parallel imaging reconstruction. The theory of phase-constrained parallel MR image reconstructions will be discussed, implementations in phantoms and in vivo will be demonstrated, and caveats and limits for practical implementation will be outlined.

2. Theory

2.1. Phase-constrained equations and image reconstruction

The central concept behind phase-constrained parallel MRI reconstruction is to exploit a priori knowledge of the image phase to reduce the number of unknowns in the reconstruction. This results in better conditioning or increased overdetermination of the matrix to be inverted. Below, we outline the central inverse problem associated with parallel MR image reconstruction, and then we describe how this equation can be modified to take advantage of prior knowledge of the image phase.

The radiofrequency (RF) MR signal induced in a given coil (indexed by l) from spin excitation in an arbitrary volume can be written, after demodulation by the Larmor frequency, as an integral of the magnetization density, ρ against the coil sensitivity, C_l, and the sinusoidal phase modulations induced by the gradient coils

$$S_l(\mathbf{k}) = \int \mathbf{dr}\rho(\mathbf{r})C_l(\mathbf{r})\mathrm{e}^{-\mathrm{i}2\pi\mathbf{k}\cdot\mathbf{r}}. \tag{1}$$

This integral equation can be discretized and written in the form of a matrix equation

$$\mathbf{S} = \mathbf{E}\rho. \tag{2}$$

Here, $\mathbf{S}$ is a vector, with elements $\mathrm{S}_p \equiv S_l(\mathbf{k})$, containing the measured signal data in all coils, where every combination of *k*-space index, $\mathbf{k}$, and coil index, l, maps onto a unique row index, p. The magnetization density is also represented by a single column vector, ρ, with elements $\rho_j \equiv \rho(\mathrm{r}_j)$, where r_j is the position of the center of voxel j. The encoding matrix, $\mathbf{E}$, which contains the coil sensitivity and gradient coil modulations, has matrix elements defined by $\mathrm{E}_{pj} \equiv C_l(\mathrm{r}_j)\exp(-\mathrm{i}2\pi\mathrm{k}\mathrm{r}_j)$, where again p indexes combinations of l and k values. Eq. (2) can be written in explicit real representation as

$$\begin{bmatrix}\mathrm{Re}(\mathbf{S})\\ \mathrm{Im}(\mathbf{S})\end{bmatrix} = \begin{bmatrix}\mathrm{Re}(\mathbf{E}) & -\mathrm{Im}(\mathbf{E})\\ \mathrm{Im}(\mathbf{E}) & \mathrm{Re}(\mathbf{E})\end{bmatrix}\begin{bmatrix}\mathrm{Re}(\rho)\\ \mathrm{Im}(\rho)\end{bmatrix}. \tag{3}$$

Eq. (3) will prove useful for comparison with an analogous phase-constrained equation below.

The complex image intensity can be written in terms of its magnitude and phase: $\rho(\mathrm{r}_j) = \hat{\rho}(\mathrm{r}_j)\exp(\mathrm{i}\varphi(\mathrm{r}_j))$, where $\hat{\rho}(\mathrm{r}_j)$ is a real quantity proportional to the magnetization density, and $\varphi(\mathrm{r}_j)$ is the image phase. We can then rewrite Eq. (2) as

$$\mathbf{S} = \mathbf{E}\rho = \mathbf{E}\mathbf{P}\hat{\rho}, \tag{4}$$

where $\rho \equiv \mathbf{P}\hat{\rho}$, $\mathbf{EP}$ is the new effective encoding matrix, and $\mathbf{P}$ is a diagonal matrix containing the common fully encoded (unaliased) phase with matrix elements defined by

$$\mathrm{P}_{jj'} \equiv \begin{cases}\mathrm{e}^{\mathrm{i}\varphi(\mathrm{r}_j)} & j = j',\\ 0 & j \neq j'.\end{cases} \tag{5}$$

Eq. (4) is a complex matrix equation, but can be written in explicit real representation as

$$\begin{bmatrix} \mathrm{Re}(\mathbf{S}) \\ \mathrm{Im}(\mathbf{S}) \end{bmatrix} = \begin{bmatrix} \mathrm{Re}(\mathbf{EP}) \\ \mathrm{Im}(\mathbf{EP}) \end{bmatrix} \hat{\rho} \tag{6}$$

or

$$\bar{\mathbf{S}} = \bar{\mathbf{E}}\hat{\rho} \quad \text{where } \bar{\mathbf{E}} \equiv \begin{bmatrix} \mathrm{Re}(\mathbf{EP}) \\ \mathrm{Im}(\mathbf{EP}) \end{bmatrix} \quad \text{and} \quad \bar{\mathbf{S}} \equiv \begin{bmatrix} \mathrm{Re}(\mathbf{S}) \\ \mathrm{Im}(\mathbf{S}) \end{bmatrix}. \tag{7}$$

The solution vector $\hat{\rho}$ in the constrained problem Eq. (6) is half the size of the solution vector in the standard problem Eq. (3), because the imaginary part of the magnetization density is assumed to be zero. Consequently, the constrained problem is twice as overdetermined as the unconstrained problem, and the level of undersampling at which the encoding matrix remains invertible is twice what it is for the unconstrained case, assuming the constraint is valid and the rows of $\bar{\mathbf{E}}$ are linearly independent (as discussed below). This means fewer lines need to be acquired. Additionally, at a given acceleration, more degrees of freedom are available for SNR optimization, which reduces noise amplification compared with the unconstrained case alone. Note also that because of the use of an encoding matrix, this method allows for a straightforward calculation of noise amplification, including any effects of the phase constraint.

Maximal SNR is achieved by using a modified Moore–Penrose pseudoinverse [3,7,27]

$$\bar{\mathbf{E}}_{\mathrm{inverse}} = \left(\bar{\mathbf{E}}^{\dagger}\bar{\Psi}^{-1}\bar{\mathbf{E}}\right)^{-1}\bar{\mathbf{E}}^{\dagger}\bar{\Psi}^{-1}, \tag{8}$$

where the superscript † represents the Hermitian adjoint and $\bar{\Psi}$ is a modified version of the noise covariance matrix representing the correlation of noise between the real and imaginary channels

$$\bar{\Psi} = \begin{bmatrix} \langle \mathrm{Re}\, n_l \mathrm{Re}\, n_{l'} \rangle & \langle \mathrm{Im}\, n_l \mathrm{Re}\, n_{l'} \rangle \\ \langle \mathrm{Re}\, n_l \mathrm{Im}\, n_{l'} \rangle & \langle \mathrm{Im}\, n_l \mathrm{Im}\, n_{l'} \rangle \end{bmatrix} \otimes \mathbf{Id}_{\mathbf{k}}. \tag{9}$$

The brackets, $\langle\rangle$, indicate a time average over noise samples, n. A subset of coil indices, l and l', is shown to indicate the matrix structure, and the direct product with the identity, $\mathbf{Id}_{\mathbf{k}}$, indicates that these elements are replicated for all k-space indices. This inversion, as it is written, is like SENSE but can be tuned to be more SMASH-like or GRAPPA-like by inverting smaller sub-blocks of the encoding matrix [7]. In practice, $\bar{\Psi}$ may be measured by acquiring noise records in all coils, (e.g., in a short noise-only scan), separating them into real and imaginary parts, and computing the relevant correlations. This procedure is essentially equivalent to the one used for unconstrained reconstructions, but with separated real and imaginary channels.

The expression for SNR in the constrained reconstruction is analogous to that for the unconstrained case. The SNR loss compared to a fully gradient-encoded image is quantified by the noise amplification factor, or geometry factor, g [3]. To calculate the g-factor, we first express the noise variance, σ_j^2, in any voxel j of the reconstructed image as the diagonal element of a transformed noise covariance matrix, as in [3]

$$\sigma^2 = \left(\bar{\mathbf{E}}_{\mathrm{inverse}}\bar{\Psi}\bar{\mathbf{E}}_{\mathrm{inverse}}^{\dagger}\right)_{jj} = \left(\bar{\mathbf{E}}^{\dagger}\bar{\Psi}^{-1}\bar{\mathbf{E}}\right)_{jj}^{-1}. \tag{10}$$

The g-factor is then proportional to the ratio of the noise standard deviation, σ_j, to the corresponding σ_j^{full}, which would have been obtained in an unaccelerated reconstruction. This ratio is scaled by the square root of the acceleration factor, R (relative to the corresponding fully sampled full-Fourier dataset), to account for a loss in temporal averaging and yield a pure measure of the SNR loss from geometric factors alone [3]

$$g = \frac{1}{\sqrt{R}}\frac{\sigma_j}{\sigma_j^{\mathrm{full}}}. \tag{11}$$

The value of σ_j in the numerator of Eq. (11) may be calculated from $\bar{\mathbf{E}}_{\mathrm{inverse}}$ and $\bar{\Psi}$ as shown in Eq. (10). The value of σ_j^{full} may be calculated using the unconstrained version of Eq. (10) with $R = 1$. For k-space trajectories on a Cartesian grid, σ_j^{full} reduces to the square root of the simplified expression in Eqs. (20–21) of [3], which can be written in the current notation as

$$\sigma_j^{\mathrm{full}} = \frac{1}{\sqrt{N_{\mathrm{pix}}}}\left(\sum_{l}\sum_{l'} C_l^{*}(\mathbf{r}_j)\Psi_{ll'}^{-1}C_{l'}(\mathbf{r}_j)\right)^{-1/2}. \tag{12}$$

Here, the elements of the standard noise resistance matrix, $\Psi_{ll'} = \langle n_l n_{l'} \rangle$, describe correlations among complex noise records, and N_{pix} is the number of pixels in the phase-encode direction.

2.2. Coil sensitivity calibration and phase estimation

The phase variations in $\mathbf{P}$ may arise from the transmit RF phase, gradient non-linearities, susceptibility variations, special techniques such as flow encoding, or various other sequence-dependent factors. Independently acquired phase information, for example from a body coil image, may be used to generate $\mathbf{P}$ for a phase-constrained (also referred to in this paper simply as constrained) reconstruction. Additional images are not, however, required. Measuring the coil sensitivities in vivo [7] can provide both the sensitivity and phase calibration in the same scan. Whether acquired simultaneously or separately, the sensitivity and phase calibration can be acquired quickly at low resolution.

For in vivo sensitivities, reference component-coil images in the target image plane are obtained from a separate acquisition or from a set of central k-space lines [28]. These images, which may be of lower spatial resolution than the target image, can be used for coil calibra-

tion but also contain information about the target object and its phase. As a result, an encoding matrix constructed using the reference images in place of the coil sensitivities will contain the phases needed for the constrained reconstruction, assuming the phase properties of the reference and acquisition scans match, and assuming the resolution of the reference set is sufficient. We can see how this works by considering the steps detailed below. Eq. (4) can formally be rewritten as

$$\mathbf{S} = \mathbf{E}^{\text{eff}}\mathbf{M}^{-1}\hat{\rho}, \tag{13}$$

where the matrix elements of $\mathbf{M}$ are defined by

$$\mathrm{M}_{jj'} \equiv \begin{cases} \hat{\rho}^{\text{ref}}(r_j) & j = j', \\ 0 & j \neq j', \end{cases} \tag{14}$$

$\hat{\rho}^{\text{ref}}$ is the magnitude of the reference magnetization density (from the reference images), and $\mathbf{E}^{\text{eff}} \equiv \mathbf{EPM}$ is the new effective encoding matrix. Note that apparent problems that arise with Eq. (13) when $\hat{\rho}^{\text{ref}}(r_j) = 0$ can be handled easily in the inversion, as this is somewhat of an artificial zero-over-zero occurrence. The pseudoinverse is based on singular value decomposition and discards singular values less than a specified tolerance (we just use machine precision). All factors originating from the reference magnetization density may be removed by post-multiplication

$$\hat{\rho} = \mathbf{M}\mathbf{E}^{\text{eff}}_{\text{inverse}}\mathbf{S}. \tag{15}$$

This is analogous to the use of in vivo sensitivities in [7]. In practice, we simply construct the encoding matrix using the reference images (rather than sensitivity maps), perform the reconstruction (multiply the signal vector by the inverted effective encoding matrix), and multiply the result by the square root of the sum of the squared reference images (this quantity approximates $\mathbf{M}$). The constrained form of Eq. (13) follows naturally:

$$\begin{bmatrix} \mathrm{Re}(\mathbf{S}) \\ \mathrm{Im}(\mathbf{S}) \end{bmatrix} = \begin{bmatrix} \mathrm{Re}(\mathbf{EPM}) \\ \mathrm{Im}(\mathbf{EPM}) \end{bmatrix} \mathrm{M}^{-1}\hat{\rho}. \tag{16}$$

2.3. k-Space trajectories and symmetry

When using this technique for improved parallel imaging alone (i.e., comparing constrained and unconstrained reconstruction, as opposed to comparison with other combined parallel and partial-Fourier algorithms), the benefits resulting from constrained versus unconstrained reconstruction depend both upon the sensitivity patterns of the coil array and upon the symmetry of the data about $k = 0$. To maximally benefit from the constraint, both the real and the imaginary parts of each encoding function (row of $\bar{\mathbf{E}}$) should be distinct. This condition breaks down if any two rows of the standard encoding matrix $\mathbf{E}$ are complex conjugates of each other—leading to a twofold degeneracy in the corresponding four lines of $\bar{\mathbf{E}}$ (lessening the overdetermination associated with the constraint). This situation can arise if the coil sensitivity $C_l(\mathbf{r})$ is purely real and if the phase encoding scheme contains pairs of conjugate k-space lines, e.g., $\{-4,-2,0,2,4\}$. Numerically real sensitivities do occur in selected circumstances, for example along an axis of symmetry oriented in the direction of the main magnetic field, but in most cases of practical interest coil sensitivities will have distinct phases, allowing improved reconstruction of full-Fourier trajectories. For numerically real sensitivities, trajectories that do not include pairs of conjugate k-space lines, e.g., $\{-5,-2,1,4\}$, guarantee distinct encoding functions, and may yield additional gains. In the general case (complex sensitivities), the distinctness of encoding functions has a more complicated dependence on coil geometry, acceleration factor, image plane orientation, and k-space trajectory.

3. Methods

Simulations were performed to test the basic theory for phase-constrained parallel image reconstruction. Simulation results were then verified with phantom and in vivo experiments.

For the simulations in Fig. 1, comparing reconstruction algorithms, a slowly varying phase (diagonal ramp from $-\pi$ to π), illustrated on the right of row (A), was imposed on a real-valued 64×64 voxel image, plotted on the left of row (A). This complex image was multiplied by coil sensitivities calculated using the Biot–Savart Law for a planar array of four loop elements. The simulated loops were 30×6 cm, spaced by 9 cm in the narrow dimension, and located 9 cm from a coronal image plane. The principal axis of the array and the phase-encode axis were oriented in the left-right direction. The FOV was 30 cm square. Gaussian noise with standard deviation of 3% of the image maximum was added to the resulting component coil images. These images were Fourier transformed, and various combinations of phase-encode lines were selected to mimic undersampled datasets. For comparison of the reconstructed image or phase, $\mathbf{I}_{\text{recon}}$, with the target image, $\mathbf{I}_{\text{target}}$, a difference image, Δ was computed using the following formula

$$\Delta = \big|\,|\,\mathbf{I}_{\text{recon}}\,| - |\,\mathbf{I}_{\text{target}}\,|\big|. \tag{17}$$

Also, for each difference image, the root-mean-square (RMS) error is quoted. The value of Δ was averaged over all pixels in the displayed region. The only exception to this is Fig. 1F, which only averaged over the central rectangular region (44×50 pixels) to exclude noise errors that are large in magnitude but insignificant to the reconstruction. Results are shown as a percentage of the reference image (or phase) maximum. For Fig. 1, $\mathbf{I}_{\text{recon}}$ was first normalized by the ratio of its mean

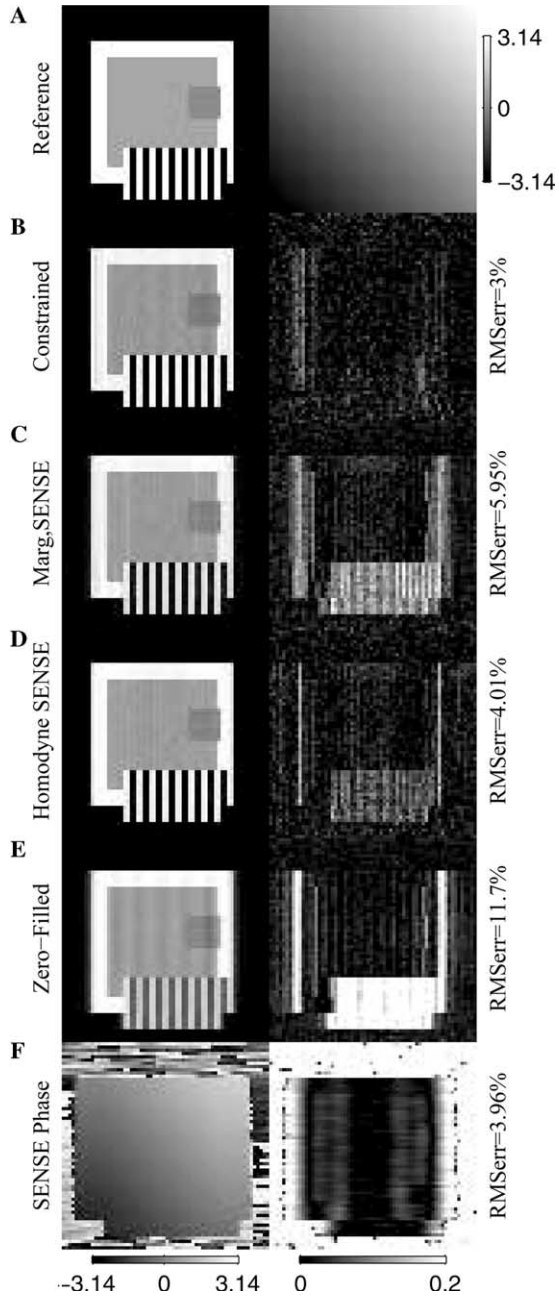

Fig. 1. Simulation comparing different combinations of partial-Fourier and parallel MRI reconstructions. The target image and phase are shown in (A) on the left and right, respectively. All reconstructions are of full-FOV 64×64 images from phase-encode lines $k = \{-8, -6 \ldots 28, 30\}$. The reconstructed image or phase is shown in the left column and the difference from the target (normalized to neglect overall magnitude errors) is shown in the right column: (B) phase-constrained reconstruction (with a low-resolution external phase calibration—lines used for calibration only, not reconstruction), (C) serial Margosian and unconstrained reconstruction, and (D) the homodyne SENSE algorithm. A zero-filled SENSE reconstruction is shown in (E) and a low-resolution phase reconstruction using SENSE is shown in (F). The phase-encode direction is left-right. All images are scaled the same relative to their own mean. RMS error values for each reconstruction are shown to the right of the difference images as a percentage of the reference image maximum (RMS error value for the phase in (F) was computed only over the central portion of the image). Colorbars for all phase images are labeled in radians.

to the mean of $\mathbf{I}_{\text{target}}$. The simulations in Fig. 1, particularly the homodyne SENSE and Margosian SENSE reconstructions, tended to have larger errors in overall magnitude, which are less significant than structured artifacts. Normalization resulted in a smaller and fairer accounting of reconstruction errors by neglecting overall magnitude differences.

The experimental data presented were acquired on a GE TwinSpeed 1.5 T imaging system with EXCITE technology (GE Medical Systems, Milwaukee, Wisconsin, USA) using fast spin echo (FSE-XL) sequences. The phantom data were acquired with TE = 42 ms, TR = 1000 ms, echo train length (ETL) = 4, bandwidth (BW) = ±31.25 kHz, FOV = 340 mm, slice thickness (TH) = 5 mm, and matrix size = 256×128 (all matrix sizes given list the frequency encoding direction first and the phase encoding direction second). The abdominal data were acquired with TE = 60 ms, TR = 1000 ms, ETL = 8, BW = ±31.25 kHz, FOV = 370 mm, TH = 5 mm, and matrix size = 256×192. The head data were acquired with TE = 85 ms, TR = 4650 ms, ETL = 16, BW = ±20.53 kHz, FOV = 220 mm, TH = 5 mm, and matrix size = 320×256. The phantom and abdominal data were acquired using a custom designed coil array (Nova Medical, Wakefield, Massachusetts, USA) with four independently positionable 89×178 mm rectangular elements and low input-impedance preamplifiers. The elements were arranged in a non-overlapping fashion in the left–right direction across the bottom of the phantom or the back of a healthy volunteer. The image plane was coronal and parallel to the array plane. The head data were acquired using the standard GE eight-channel brain coil with the elements arranged around the circumference of the head. The image plane was axial.

Two separate fully sampled data sets were acquired in each case. One was Fourier decimated to yield regularly undersampled data (e.g., for $R = 4$ in Fig. 2, every fourth phase-encode line was used, for a total of 32) or partial-Fourier style data. The other data set was used for coil sensitivity and phase calibration. This method provides an identical target image for various sampling and reconstruction schemes, while in theory mimicking the exact behavior of directly acquired aliased data (except that the relaxation properties may differ for multi-echo excitation sequences—such as those used in this article—for which the potential benefits of accelerated acquisition resulting from reduced T_2 decay are likely to be *understated*). Having a common target image allows a more straightforward comparison of the performance of various reconstruction techniques. The calibrations for Fig. 2 and Table 1 employed full resolution along the phase-encode direction. Calibration data for Figs. 3 and 4 had one-half the spatial resolution of the undersampled data in the phase-encode direction. Calibration data for Fig. 5 had one-quarter the spatial

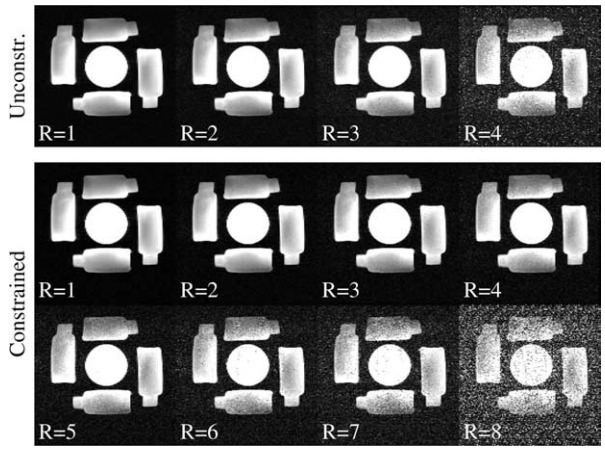

Fig. 2. Phantom images from constrained parallel reconstructions (bottom two rows) of four-channel data with acceleration factor, R, of 1 through 8. Unconstrained reconstructions are shown in the top row for R of 1 through 4. All examples shown are symmetrically undersampled.

Table 1
Changes in SNR with increasing acceleration factor, R (relative to fully sampled full-Fourier trajectory), for in vivo data

	$R=1$	$R=2$	$R=3$	$R=4$
Unconstrained SNR, $\left\langle \frac{\mathrm{SNR}}{\mathrm{SNR}^{(R=1)}} \right\rangle_{\mathrm{pix}}$	1	0.643	0.417	0.244
Constrained SNR, $\left\langle \frac{\mathrm{SNR}}{\mathrm{SNR}^{(R=1)}} \right\rangle_{\mathrm{pix}}$	1	0.675	0.500	0.372
Change in SNR, $\left\langle \frac{\mathrm{SNR}^{\mathrm{pc}}}{\mathrm{SNR}^{\mathrm{uc}}} \right\rangle_{\mathrm{pix}}$	1	1.06	1.24	2.05

The 1st and 2nd rows show the degradation in average SNR relative to the baseline ($R=1$) images using unconstrained and phase-constrained reconstructions respectively see Eq. (18). The 3rd row shows the average increase in SNR of the phase-constrained reconstruction (pc) versus the unconstrained reconstruction (uc) [see Eq. (19)]. All calculations show relative changes that result from noise amplification (g-factor) alone, and all examples were symmetrically undersampled.

resolution of the undersampled data in the phase-encode direction. Difference images in each case were generated as in Eq. (17).

Images were produced using both phase-constrained and unconstrained reconstructions. The traditional encoding matrix $\mathbf{E}$ or the constrained encoding matrix $\bar{\mathbf{E}}$ was formed as outlined in the *Theory* section, inverted, and multiplied by the appropriate signal vector to yield an image. A serial combination of standard Margosian [11] and unconstrained reconstructions was used for Fig. 1C. The algorithm used for Figs. 1D, 3E, 4E, and 5D using homodyne detection with SENSE, is described in [22]. First, the high spatial frequency data were doubled to compensate for only having half of the high frequency components, a ramp filter was used for the central portion of the data to reduce Gibbs artifacts by imposing a smooth transition from 0 to 2, and a set of partial FOV aliased coil images was generated. Then two SENSE reconstructions were performed, one on these partial FOV images, and one on the corresponding

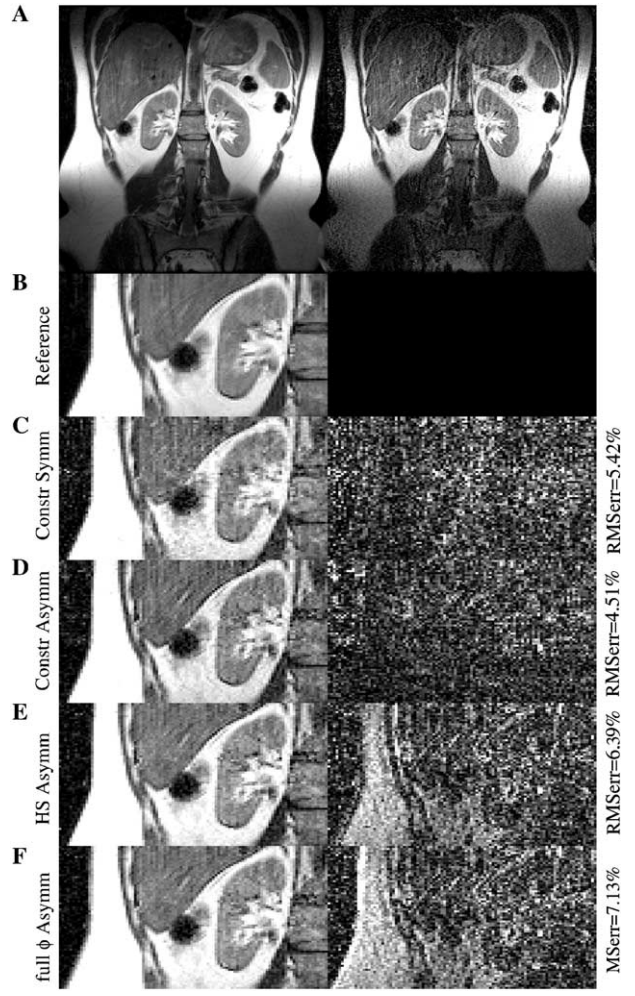

Fig. 3. Comparison of various 5-fold accelerated reconstructions using four-coil in vivo data. The fully sampled reconstruction is shown on the left in (A). The image in the right column of (A) is a phase-constrained reconstruction using phase-encode lines $k=\{-21,-18,-15,\ldots 90,93\}$ (partial-Fourier style data with 3-fold undersampling) and an external half-resolution coil and phase calibration. Close-ups of the region near the right kidney are shown in the lower portion of the figure for various sampling and reconstruction methods. The reconstructed image is shown in the left column, and the difference from the fully sampled target image is shown in the right column: (B) fully sampled reference reconstruction, (C) phase-constrained reconstruction of regularly undersampled data with 5-fold undersampling $k=\{-96,-91,-86,\ldots 89,94\}$ and half-resolution coil and phase calibration, (D) phase-constrained reconstruction of partial-Fourier style data with 3-fold undersampling $k=\{-21,-18,-15,\ldots 90,93\}$ and half-resolution coil and phase calibration, (E) homodyne SENSE reconstruction of the same data as in (D), and (F) homodyne SENSE reconstruction of the same data as in (D) using a full-resolution external phase calibration. The phase-encode direction is left-right. All comparable images are scaled the same. RMS error values for each reconstruction are shown to the right of the difference images as a percentage of the reference image maximum.

low resolution partial FOV images. The phase of the low resolution SENSE reconstruction was used for phase correction of the full resolution reconstruction.

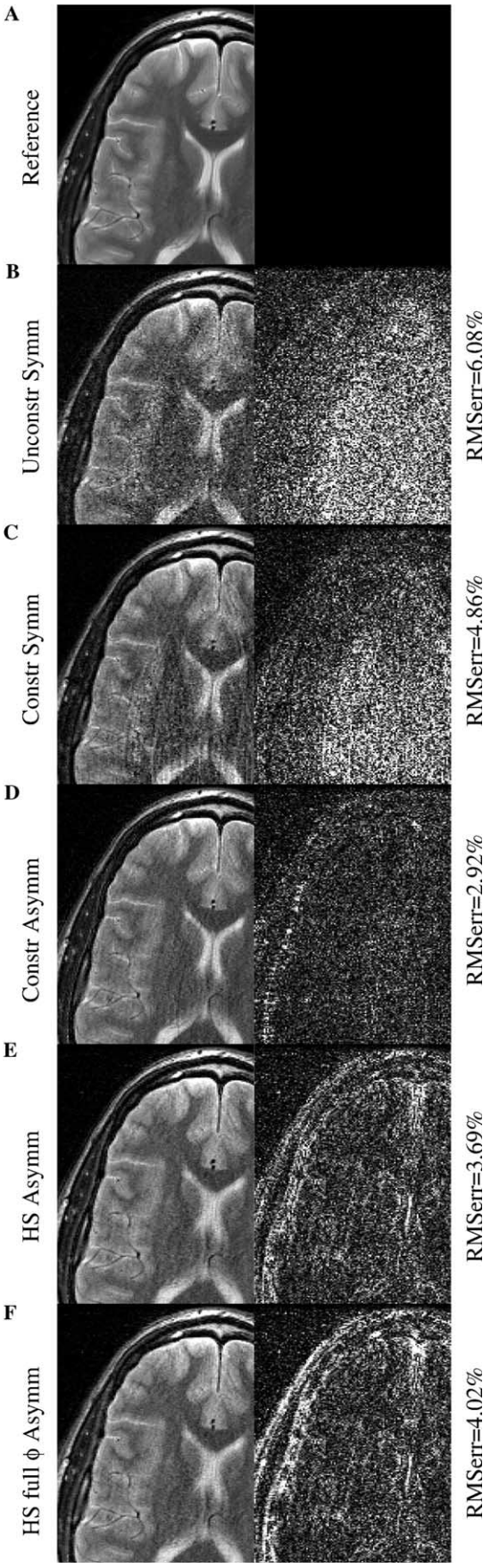

Changes in SNR relative to baseline ($R = 1$) images that result from noise amplification can be computed from the inverse of the ratio of noise levels, $\mathrm{SNR}/\mathrm{SNR}^{\mathrm{full}} = \sigma^{\mathrm{full}}/\sigma$ [3]. The g-factor already contains this information (Eq. (11)), and thus was used to compute the decreases in SNR shown in Table 1 (see Eq. (24) from [3]):

$$\left\langle \frac{\mathrm{SNR}}{\mathrm{SNR}^{(R=1)}} \right\rangle_{\mathrm{pix}} = \left\langle \frac{1}{g} \right\rangle_{\mathrm{pix}} \frac{1}{\sqrt{R}}. \tag{18}$$

Here, the angle brackets represent an average over all pixels. Average increases in SNR resulting from application of the phase constraint were computed by averaging a pixel-by-pixel ratio of the unconstrained to constrained g-factor maps over the image plane

$$\left\langle \frac{\mathrm{SNR}^{\mathrm{pc}}}{\mathrm{SNR}^{\mathrm{uc}}} \right\rangle_{\mathrm{pix}} = \left\langle \frac{g^{\mathrm{uc}}}{g^{\mathrm{pc}}} \right\rangle_{\mathrm{pix}}, \tag{19}$$

where pc (uc) stands for phase-constrained (unconstrained). g-factor maps were calculated using Eq. (11). For unaccelerated magnitude images, the SNR was calculated by selecting signal and noise-only regions and accounting for the Rician distribution of noise using the methods in [29].

All calculations were performed using MATLAB Version 7, Release 14 (The MathWorks, Natick, MA) on a Macintosh PowerBook G4 with 1 GHz processor and 1.25 GB DDR SDRAM memory. Code for reconstruction was not necessarily optimized, but we provide here some example reconstruction times for reference. The Margosian SENSE, homodyne SENSE, and phase-constrained reconstructions shown in Fig. 1 took 14.5, 39.1, and 9.84 s, respectively. The full-Fourier constrained, partial-Fourier constrained, and homodyne SENSE reconstructions in Fig. 3 (rows C–E) took 64.2, 82.6, and 85.4 s, respectively. The SENSE, full-Fourier constrained, partial-Fourier constrained, and homodyne SENSE reconstructions in Fig. 4 (rows

Fig. 4. Comparison of various 5-fold accelerated reconstructions using eight-coil in vivo data. All images are cropped to show better detail. The reconstructed image is shown in the left column, and the difference from the fully sampled target image is shown in the right column: (A) fully sampled reference reconstruction, (B) unconstrained reconstruction of regularly undersampled data with 5-fold undersampling $k = \{-128, -123, -118, \ldots 122, 127\}$ and half-resolution external coil calibration, (C) phase-constrained reconstruction of the same data as in (B) with half-resolution external coil and phase calibration, (D) phase-constrained reconstruction of partial-Fourier style data with 3-fold undersampling $k = \{-27, -24, -21, \ldots 123, 126\}$ and half-resolution external coil and phase calibration, (E) homodyne SENSE reconstruction of the same data as in (D), and (F) homodyne SENSE reconstruction of the same data as in (D) using a full-resolution external phase calibration. The phase-encode direction is left-right. All comparable images are scaled the same. RMS error values for each reconstruction are shown to the right of the difference images as a percentage of the reference image maximum.

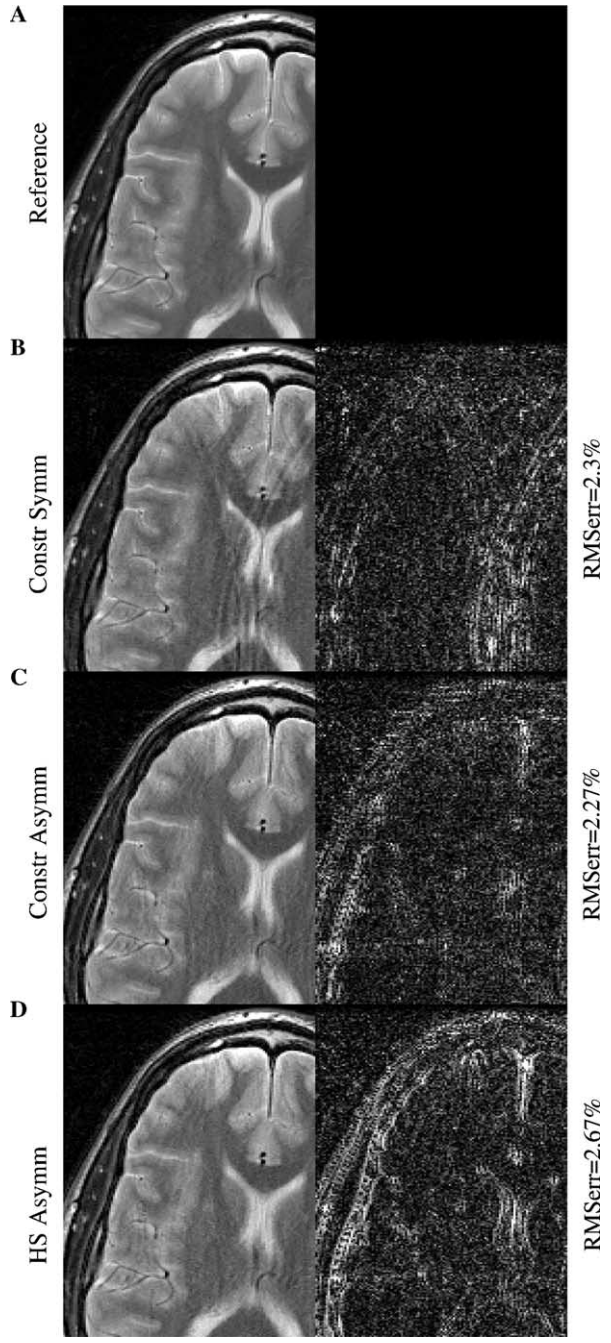

Fig. 5. Comparison of various 3-fold accelerated reconstructions using eight-coil in vivo data and low-resolution calibration. All images are cropped to show better detail. The reconstructed image is shown in the left column, and the difference from the fully sampled target image is shown in the right column: (A) fully sampled reference reconstruction, (B) phase-constrained reconstruction of regularly undersampled data with 3-fold undersampling $k = \{-128, -125, -122, \ldots 124, 127\}$ and quarter-resolution external phase and coil calibration, (C) phase-constrained reconstruction of partial-Fourier style data with 2-fold undersampling $k = \{-44, -42, -40, \ldots 124, 126\}$ (still net acceleration factor of 3) and quarter-resolution external coil and phase calibration, and (D) homodyne SENSE reconstruction of the same data as in (C). The phase-encode direction is left-right. All comparable images are scaled the same. RMS error values for each reconstruction are shown to the right of the difference images as a percentage of the reference image maximum.

B–E) took 259, 237, 144, and 159 s, respectively. The times quoted for Figs. 3 and 4 correspond to the use of a standard fast conjugate gradient approach for inversion (not optimized for real matrix inversion). Each comparison utilizes the same numerical inversion technique consistently for all reconstructions.

4. Results

Fig. 1 demonstrates how a simple serial combination of partial-Fourier and image-space parallel reconstructions can introduce errors. The target image (left) and phase (right) are shown in row (A). In this case, the Margosian reconstruction of an aliased image generates errors that propagate through the unconstrained parallel reconstruction (C) (seen in this case as magnitude errors, edge artifacts, and a smearing or loss of resolution in the phase encode direction), even though the full-FOV image phase is slowly varying. Similar, but smaller, errors are seen using a combination of homodyne and unconstrained parallel reconstructions (D) [22]. For completeness, a zero-filled SENSE reconstruction without any masking (E) and the SENSE reconstructed phase (F) are shown. The actual homodyne SENSE algorithm shown in (D) multiplies the zero-filled data by a mask prior to reconstruction that softens the severe transition to zero entries and doubles the asymmetric high frequency data. These errors do not appear, however, in the phase-constrained parallel reconstruction of the same k-space lines, seen in (B). The central eight lines of the phase were used for calibration of the constrained reconstruction—the same number of lines used by the Margosian and homodyne reconstructions (even-numbered lines of the central 16). We should clarify that lines used for calibration were not added to the dataset to be included in the reconstruction. All reconstructions used the same phase encode lines, $k = \{-8, -6, \ldots 28, 30\}$ out of 64 total. The simulated phase here is slowly varying—mostly, but not exactly, specified in the central eight lines of the Fourier transform.

Fig. 2 displays phase-constrained reconstructions of four-coil phantom data with acceleration factors ranging from one to eight. Each image uses symmetrically sampled data (standard regular undersampling as opposed to partial-Fourier style undersampling, but also symmetrically indexed about $k = 0$). Unconstrained images for R of one to four show the usual degradation in SNR as the acceleration factor approaches the total number of coils. In comparison, the constrained reconstructions show a more gradual degradation in apparent SNR as the acceleration factor is increased. Additionally, the constrained reconstructions here remain artifact-free up to $R = 8$ (twice the coil count).

Fig. 3 compares various $R = 5$ reconstructions of the abdominal in vivo data using four coils. A 5-fold accelerated phase-constrained reconstruction using phase encode lines $k = \{-21, -18, -15 \ldots 90, 93\}$ is shown on the right in row (A) compared to a fully sampled reference image on the left. A cropped region of this image is shown for various other sampling and reconstruction methods. Reconstructed images are shown in the left column. Difference images (with respect to the reference image) are shown in the right column. Row (B) is the reference image, row (C) is a phase-constrained reconstruction of full-Fourier undersampled data with $R = 5$, $k = \{-96, -91 \ldots 89, 94\}$, row (D) is a phase-constrained reconstruction of partial-Fourier style data with line spacing of 3 (still net acceleration of 5), $k = \{-21, -18, -15, \ldots 87, 90, 93\}$, row (E) is a homodyne SENSE reconstruction of the same data as in (D), row (F) is a homodyne SENSE reconstruction of the same data as in (D) but using a full-resolution external phase calibration. The constrained reconstructions in (C) and (D) both use a half-resolution (96 out of 192 phase encode lines) coil and phase calibration.

Rows one and two of Table 1 quantify, for this in vivo abdominal dataset, the decrease in average SNR at acceleration factors of one to four resulting from g-factor alone (described above and seen qualitatively in Fig. 2). These reconstructions correspond to those illustrated in Fig. 2, but for in vivo data. All data are full-Fourier but regularly undersampled. The numbers presented are relative to the SNR of the respective $R = 1$ reconstruction for each method, estimated to be 94 and 131 for the unconstrained and constrained methods, respectively. This difference results from a noise filtering effect (discussed later) intentionally excluded from these calculations. Row three of Table 1 illustrates the average increase in SNR from applying the constraint for $R = 1$–4, again only including g-factor effects. Note that Fig. 2 and Table 1 show results for symmetric sampling schemes only.

Fig. 4 compares various $R = 5$ reconstructions of in vivo head data using eight channels. To improve the visibility of smaller details, only a cropped portion of the reconstructed image is shown. Reconstructions are shown in the left column, and difference images (compared to reference) are shown in the right column. Row (A) is a fully sampled reference image, row (B) is a standard unconstrained (SENSE) reconstruction of full-Fourier $R = 5$ data, $k = \{-128, -123 \ldots 122, 127\}$, row (C) is a phase-constrained reconstruction of the same data as in (B), row (D) is a phase-constrained reconstruction of partial-Fourier style data with a phase-encode line spacing of 3, $k = \{-27, -24 \ldots 123, 126\}$, row (E) is a homodyne SENSE reconstruction of the same data as in (D), and row (F) is a homodyne SENSE reconstruction of the same data as in (D) but using a full-resolution external phase calibration. The reconstructions in (B–D) use half-resolution coil and phase (for constrained cases only) calibrations.

Fig. 5 illustrates errors that result from inaccurate phase calibration and reiterates the impact of the choice of phase encode scheme, particularly for low-resolution calibration. The same data as in Fig. 4 was reconstructed with one-quarter resolution phase and coil calibration (64 out of 256 lines) and a net acceleration factor of 3. The cropped portion of the reference image is shown in row (A). The constrained reconstruction of full-Fourier style data (every 3rd line) is shown in row (B), $k = \{-128, -125 \ldots 124, 127\}$. The constrained reconstruction of partial-Fourier style data, still with net acceleration factor of three, but skipping only every other line is shown in row (C), $k = \{-44, -42 \ldots 124, 126\}$. Row (D) contains a homodyne SENSE reconstruction of the same data as in (C).

5. Discussion

The phase-constrained parallel image reconstruction method presented in this paper provides a novel combination of partial-Fourier and parallel imaging techniques with a rigorous incorporation of the phase constraint and is capable of avoiding errors arising from partial-Fourier reconstruction of aliased images. The potential for these errors is illustrated in Fig. 1. The example of Fig. 1 is not necessarily representative of all coils, objects, or phases, but it provides motivation for further exploration.

From the point of view of partial-Fourier imaging, our reconstruction can be viewed as a generalized phase-constrained reconstruction with coil sensitivities included as prior information. From the point of view of parallel imaging, the constraint assists in generating skipped lines in a new way—through conjugate symmetry. For traditional partial-Fourier trajectories (i.e., for trajectories with sampling omitted on one side of k-space), use of this conjugate symmetry provides essentially the same result as a straightforward combination of parallel MRI with partial-Fourier reconstruction (assuming that such a combination is successful). However, the generalized form of the reconstruction proposed here is compatible with many different types of undersampled k-space trajectories. For example, we have shown results using full-Fourier trajectories (i.e., both sides of k-space sampled) which are either symmetric or asymmetric about $k = 0$. Variable-density trajectories (such as those used in self-calibrating reconstructions) can also be used. Even non-Cartesian trajectories should be possible with this formalism, though we have not tested any.

For the purposes of exploring this new reconstruction, we have chosen in some cases to compare its performance to standard full-Fourier SENSE recon-

struction. This serves as a good reference point for which we can quantify meaningful performance related factors such as SNR and noise amplification. We have demonstrated that, as expected, when a phase constraint is imposed on parallel MRI reconstructions, lower noise amplifications (see Fig. 2 and Table 1) and higher achievable net acceleration factors (see Fig. 2) are observed.

For full-Fourier trajectories that are pair-wise asymmetrically sampled (have unpaired conjugate lines, as opposed to the asymmetry of partial-Fourier sampling), some reduction in noise amplification can be achieved by combining partial-Fourier and parallel MR reconstructions in two steps. The interlaced placement of acquired and corresponding conjugate lines allows the filling of lines using symmetry alone. In symmetrically sampled cases, however, such as Fig. 2 or Table 1, Margosian or homodyne algorithms cannot generate any missing lines, and the improvements result only from the combined effects of coil sensitivity information (mixing predominantly nearby k-space lines) and conjugate symmetry (mixing only conjugate lines). For such trajectories, one might consider using a more general partial-Fourier algorithm, such as POCS, in combination with parallel imaging. Such a combination, however, would also not involve simple sequential application of existing techniques. The POCS-SENSE algorithm [26], for example, requires recasting the parallel image reconstruction in terms of an iteratively applied projection.

Phase-constrained parallel MRI reconstruction offers an alternative to the combination of homodyne detection and SENSE employed on many scanners (which by and large we found to be quite robust, certainly more so than serial Margosian and SENSE reconstructions). These two techniques generally performed similarly, with a few exceptions (comparing identical trajectories). Homodyne SENSE artifacts typically appeared as edge effects and loss in resolution (e.g., Fig. 4E, errors at edges in the brain or at the center of the CSF). Phase-constrained artifacts typically appeared as aliasing effects (e.g., Figs. 4C and D and Fig. 5B, repetition of the curved edge of the head), signal dropout where the phase calibration was inaccurate, or noise amplification related to the coil sensitivities and reconstruction (g-factor). The often-structured appearance of artifacts from phase-constrained reconstruction makes them more distracting to the eye but could make them tolerable compared to a general loss in resolution if they are located (by accident or design) in a region of reduced interest. Key benefits of the constrained approach, however, are its one-step reconstruction and its flexibility in choice of sampling trajectories.

The constrained reconstruction extracts the phase map from the sensitivity calibration, which already must be acquired for any combination of partial-Fourier and parallel MRI. We have illustrated situations for which the homodyne algorithm, even with exact or full-resolution phase information (Figs. 3 and 4), resulted in greater errors than the constrained approach. This was because of errors introduced by the conjugate doubling step of the homodyne algorithm. On the other hand, the phase-constrained reconstruction can produce stronger localized noise amplification and more noticeable aliasing artifacts in some situations. We note, in passing, that the errors for homodyne SENSE with full-resolution phase calibration appear larger than those with low-resolution phase calibration. This could be because the calibration was taken from a separate acquisition—making the high-resolution information especially susceptible to motion or misalignment problems. The high-resolution calibration also has more noise, which could impact the overall noise level and RMS error of the reconstruction.

As expected, for high accelerations, combinations of partial-Fourier like trajectories with lower parallel accelerations, using constrained reconstruction *or* the homodyne algorithm, generally performed better than constrained reconstruction with regular undersampling and larger parallel acceleration (i.e., combining partial-Fourier with two-fold undersampling versus four-fold regular undersampling). This is particularly true for low-resolution phase calibration. The phase-constrained reconstruction of regularly undersampled data generally demonstrated more aliasing artifacts and more severe sensitivity to phase errors than a combination of partial-Fourier sampling with a lower parallel acceleration. Aliasing ghosts from parallel reconstruction can be more conspicuous than the diffuse artifacts or loss in resolution that other partial-Fourier techniques produce. However, the generality of the phase-constrained reconstruction enables the use of the better performing partial-Fourier type trajectory with a single one-step constrained reconstruction. Other trajectories remain to be investigated further.

Phase-constrained reconstruction gives improved SNR compared with unconstrained reconstruction even for $R = 1$ images, despite identical unitary g-factors. The constrained inversion intrinsically eliminates the imaginary channel noise. This results in an approximate $\sqrt{2}$ reduction in noise as compared with an unconstrained magnitude image containing noise from both real and imaginary channels. Of course, the component of the improvement in SNR that results from noise filtering could also be accomplished by rephasing an unconstrained reconstruction and taking its real part. This baseline improvement, then, is not unique to the constrained case, and it was excluded from the calculations for Table 1. One benefit of the constrained technique, however, is that this rephasing occurs automatically.

An effort should be made to guarantee the accuracy of the phase calibration for constrained reconstruction,

because of the potential for errors. Ideally, the underlying phase should be slowly varying and motion between the calibration and the accelerated scan should be minimized. Tissue interfaces with large susceptibility discontinuities can result in rapid phase variations, posing problems for low-resolution phase maps. The number of phase calibration lines required depends on many factors and was not specifically explored in this study. The limitations of phase calibration need to be explored further, along with possible solutions such as phase extrapolation or smoothing. Nonetheless, when using modest parallel acceleration factors with partial-Fourier type sampling (as opposed to full-Fourier but highly undersampled schemes), the constrained reconstruction seems to be robust, even with low-resolution calibration.

6. Conclusions

We have presented data to illustrate specific benefits of phase-constrained parallel image reconstructions. The general formalism of the technique enables the combination of partial-Fourier and parallel MR imaging into a single-step exact-inversion method and enables the use of atypical sampling schemes that cannot be handled using traditional combinations of parallel MRI and partial-Fourier reconstructions. Constrained reconstruction improves SNR compared to unconstrained reconstruction without partial-Fourier and allows the extension of achievable undersampling factors beyond the total number of coils used, even for trajectories that would not normally allow additional acceleration using partial-Fourier techniques. This technique can also be used to avoid potential errors introduced by serial combinations of partial-Fourier and SENSE-like reconstructions. Finally, phase-constrained reconstruction offers a more streamlined and flexible alternative to combined homodyne and SENSE reconstructions.

Acknowledgments

J.D.W. acknowledges fellowship support from NIH Training Grant 5T32HL07374-23. Additional support for this work was provided by NIH Grants R29 HB60802 and R01 EB00447.

References

[1] D.K. Sodickson, W.J. Manning, Simultaneous acquisition of spatial harmonics (SMASH): fast imaging with radiofrequency coil arrays, Magn. Reson. Med. 38 (1997) 591–603.
[2] P.M. Jakob, M.A. Griswold, R.R. Edelman, D.K. Sodickson, AUTO-SMASH: a self-calibrating technique for SMASH imaging, MAGMA 7 (1998) 42–54.
[3] K.P. Pruessmann, M. Weiger, M.B. Scheidegger, P. Boesiger, SENSE: sensitivity encoding for fast MRI, Magn. Reson. Med. 42 (1999) 952–962.
[4] M.A. Griswold, P.M. Jakob, M. Nittka, J.W. Goldfarb, A. Haase, Partially parallel imaging with localized sensitivities (PILS), Magn. Reson. Med. 44 (2000) 602–609.
[5] W.E. Kyriakos, L.P. Panych, D.F. Kacher, C.F. Westin, S.M. Bao, R.V. Mulkern, F.A. Jolesz, Sensitivity profiles from an array of coils for encoding and reconstruction in parallel (SPACE RIP), Magn. Reson. Med. 44 (2000) 301–308.
[6] D.K. Sodickson, Tailored SMASH image reconstructions for robust in vivo parallel MR imaging, Magn. Reson. Med. 44 (2000) 243–251.
[7] D.K. Sodickson, C.A. McKenzie, A generalized approach to parallel magnetic resonance imaging, Med. Phys. 28 (2001) 1629–1643.
[8] R.M. Heidemann, M.A. Griswold, A. Haase, P.M. Jakob, VD-AUTO-SMASH imaging, Magn. Reson. Med. 45 (2001) 1066–1074.
[9] M.A. Griswold, P.M. Jakob, R.M. Heidemann, M. Nittka, V. Jellus, J. Wang, B. Kiefer, A. Haase, Generalized autocalibrating partially parallel acquisitions (GRAPPA), Magn. Reson. Med. 47 (2002) 1202–1210.
[10] Z.-P. Liang, F.E. Boada, R.T. Constable, E.M. Haacke, P.C. Lauterbur, M.R. Smith, Constrained reconstruction methods in MR imaging, Rev. Magn. Reson. Med. 4 (1992) 67–185.
[11] P. Margosian, F. Schmitt, D.E. Purdy, Faster MR imaging: imaging with half the data, Health Care Instrum. 1 (1986) 195–197.
[12] D.C. Noll, D.G. Nishimura, A. Macovski, Homodyne detection in magnetic resonance imaging, IEEE Trans. Med. Imaging MI-10 (1991) 154–163.
[13] J.J. Cuppen, A. Van Est, Reducing MR imaging time by one-sided reconstruction., Topical Conf. Fast MRI Techniques, Cleveland, Ohio (1987).
[14] D.C. Youla, H. Webb, Image restoration by the method of convex projections: Part 1—theory, IEEE Trans. Med. Imaging MI-1 (1982) 81–94.
[15] M.I. Sezan, H. Stark, Image restoration by the method of convex projections: Part 2—applications and numerical results, IEEE Trans. Med. Imaging MI-1 (1982) 95–101.
[16] M.I. Sezan, H. Stark, Tomographic image reconstruction from incomplete view data by complex projections and direct Fourier inversion, IEEE Trans. Med. Imaging MI-3 (1984) 91–98.
[17] M. Weiger, K.P. Pruessmann, P. Boesiger, Cardiac real-time imaging using SENSE, Magn. Reson. Med. 43 (2000) 177–184.
[18] M.A. Griswold, P.M. Jakob, Q. Chen, J.W. Goldfarb, W.J. Manning, R.R. Edelman, D.K. Sodickson, Resolution enhancement in single-shot imaging using simultaneous acquisition of spatial harmonics (SMASH), Magn. Reson. Med. 41 (1999) 1236–1245.
[19] R.M. Heidemann, M.A. Griswold, B. Kiefer, M. Nittka, J. Wang, V. Jellus, P.M. Jakob, Resolution enhancement in lung 1H imaging using parallel imaging methods, Magn. Reson. Med. 49 (2003) 391–394.
[20] B.S. Li, Q. Chen, W. Li, A. Lingamneni, J.A. Polzin, R.R. Edelman, Whole-heart coverage in a single breathhold using single-shot FIESTA, 4X SENSE and half-Fourier MRI, Radiological Society of North America, (2002) 454.
[21] M. Klarhofer, B. Dilharreguy, P. van Gelderen, C.T.W. Moonen, A PRESTO-SENSE sequence with alternating partial-Fourier encoding for rapid susceptibility-weighted 3D MRI time series, Magn. Reson. Med. 50 (2003) 830–838.
[22] K.F. King, L. Angelos, SENSE with partial-Fourier homodyne reconstruction, in: Eighth Scientific Meeting of the International Society for Magnetic Resonance in Medicine, Denver, Colorado, USA, 2000, p. 153.

[23] J.D. Willig-Onwuachi, E.N. Yeh, A.K. Grant, M.A. Ohliger, C.A. McKenzie, D.K. Sodickson, Phase-constrained parallel MR image reconstruction: using symmetry to increase acceleration and improve image quality, in: Eleventh Scientific Meeting of the International Society for Magnetic Resonance in Medicine, Toronto, Ontario, Canada, 2003, p. 19.
[24] M. Bydder, M.D. Robson, Partial Fourier partially parallel imaging, in: Twelfth Scientific Meeting of the International Society for Magnetic Resonance in Medicine, Kyoto, Japan, 2004, p. 532.
[25] C. Lew, D. Spielman, R. Bammer, TurboSENSE: phase estimation in temporal phase-constrained parallel imaging, in: Twelfth Scientific Meeting of the International Society for Magnetic Resonance in Medicine, Kyoto, Japan, 2004, p. 2646.
[26] A. Samsonov, E. Kholmovski, C. Johnson, Phase-constrained reconstructon of sensitivity-encoded MRI data with POCSENSE, in: Twelfth Scientific Meeting of the International Society for Magnetic Resonance in Medicine, Kyoto, Japan, 2004, p. 2647.
[27] E.W. Weisstein, Moore-Penrose matrix inverse, From MathWorld–A Wolfram Web Resource, Available from: <http://mathworld.wolfram.com/Moore-PenroseMatrixInverse.html>.
[28] C.A. McKenzie, E.N. Yeh, M.A. Ohliger, M.D. Price, D.K. Sodickson, Self-calibrating parallel imaging with automatic coil sensitivity extraction, Magn. Reson. Med. 47 (2002) 529–538.
[29] C.D. Constantinides, E. Atalar, E.R. McVeigh, Signal-to-noise measurements in magnitude images from NMR phased arrays, Magn. Reson. Med. 38 (1997) 852–857.